Li, Y. et al. (2018). Characterization of macropore structure of Malan loess in NW China based on 3D pipe models constructed by using computed tomography technology. Journal of Asian Earth Studies, 154: 271 – 279.
http://dx.doi.org/10.1016/j.jseaes.2017.12.028

Characterization of macropore structure of Malan loess in NW China based on 3D pipe models constructed by using computed tomography technology

Yanrong Li, Shengdi He, Xiaohong Deng and Yongxin Xu

Abstract

Malan loess is a grayish yellow or brownish yellow, clastic, highly porous and brittle late Quaternary sediment formed by the accumulation of windblown dust. The present-day pore structure of Malan loess is crucial for understanding the loessification process in history, loess strengths and mechanical behavior. This study employed a modern computed tomography (CT) device to scan Malan loess samples, which were obtained from the east part of the Loess Plateau of China. A sophisticated and efficient workflow for processing the CT images and constructing 3D pore models was established by selecting and programming relevant mathematical algorithms in MATLAB, such as the maximum entropy method, medial axis method, and node recognition algorithm. Individual pipes within the Malan loess were identified and constructed by partitioning and recombining links in the 3D pore model. The macropore structure of Malan loess was then depicted using quantitative parameters. The parameters derived from 2D images of CT scanning included equivalent radius, length and aspect ratio of pores, porosity, and pore distribution entropy, whereas those derived from the constructed 3D structure models included porosity, coordination number, node density, pipe radius, length, length density, dip angle, and dip direction. The analysis of these parameters revealed that Malan loess is a strongly anisotropic geomaterial with a dense and complex network of pores and pipes. The pores discovered on horizontal images, perpendicular to the vertical direction, were round and relatively uniform in shape and size and evenly distributed, whereas the pores discovered on vertical images varied in shape and size and were distributed in clusters. The pores showed good connectivity in vertical direction and formed vertically aligned pipes but displayed weak connectivity in horizontal directions. The pipes in vertical direction were thick, long, and straight compared with those in horizontal directions. These results were in good agreement with both numerical simulation and laboratory permeability tests, which indicate that Malan loess is more permeable in the vertical direction than in the horizontal directions.

1. Introduction

Loess, a grayish yellow or brownish yellow, clastic, highly porous, brittle sediment formed by the accumulation of windblown dust, covers approximately 6% of the earth's land area. In China, loess mantles about 6.7% land area, and it is mainly distributed in Shanxi, Shaanxi,

Ningxia, and Gansu, comprising the Loess Plateau of China (LPC). A typical profile of loess-paleosol sequences in the LPC consists of Wucheng loess (Q_1), Lishi loess (Q_2), and Malan loess (Q_3) from the bottom up. The present-day structure of loess results from the loessification processes (Smalley et al., 2006), and it determines the mechanical behavior and engineering properties (e.g., shear, compression and tensile strengths, and collapsibility) (Matalucci et al., 1970; Lei, 1988; Terzaghi et al., 1996).

The structure of loess pores has been investigated via optical microscopy since the middle of last century. Zhu (1963) reported a great number of macropores in superficial Malan loess collected from the middle reaches of the Yellow River. He attributed these pores to plant roots. Tan (1988) found that the loess in Lanzhou, China, is porous with a void ratio greater than 1, and macropores tend to connect to one another to form channels. Yang (1989) used a polarizing microscope and found that saturation-induced collapse causes a significant decrease in pores greater than 0.054 mm, and it influences the content of smaller pores to a limited extent.

The use of scanning electron microscopy (SEM) and mercury intrusion porosimetry (MIP) gradually led to advances in quantitative examination of loess pores since late last century. Using SEM, Gao (1988) found that the pore structure of loess is significantly different in different places. In the northwest of the LPC, the pores in Malan loess are formed by weak cementation in between silts, sands, and aggregates. The cementation is mainly provided by crystalline carbonate. In southeast of the LPC, the bond between grains (silts, sands, and aggregates) is provided by clay minerals and crystalline carbonate. This type of bonding is relatively strong, and the overall structure is more stable than that in the northwest. Li et al. (2016) indicated that most macropores in loess exist in between aggregates, whereas micropores accumulate within aggregates. Ng et al. (2017) found that the accumulation of clay particles around silt grains also form a large number of small pores.

Lin (1990) analyzed the size distribution of loess pores by MIP and SEM, and indicated that the content of macro- and meso-pores decreases with depth along a loess-paleosol sequence. Liu (1999) analyzed the images of pre- and post-liquefied loess using SEM and image processing techniques. His results showed that liquefaction causes the number of macro- (> 0.060 mm) and meso-pores (0.005–0.016 mm) to decrease, whereas that of microscopic pores (< 0.004 mm) significantly increases. Hu et al. (2001) used SEM and a self-developed image processing program, and their results indicated that the pore size decreases with the compaction degree. Deng et al. (2007) found that the seismic vibration causes a dramatic decrease of macropores. The same conclusion was made by Cai and Dong (2011) when they conducted dynamic compaction tests on loess in laboratory.

In recent years, researchers attempted to use computed tomography (CT) to reconstruct the 3D pore structure of geomaterials (Perret et al., 1999). Zhou et al. (2013) found that the pore structure obviously differs between soils subjected to different types of fertilization practices via construction of a 3D pore-throat-network and examination of 3D parameters (porosity, path length distribution, and tortuosity). Yang et al. (2014) found that the pore

size distribution of packed ore particles obeys lognormal or Gauss distribution via examination of 3D pore parameters. Based on CT scanning, Li et al. (2017) investigated the differences in 3D pore networks between bituminous coals and anthracite coals. Despite these attempts of applying CT technology on geomaterials, sophisticated 3D models that can finely depict the structure of pores in loess are lacking. This scenario is partially due to the difficulties to prepare undisturbed, small but representative loess specimens (loess is fragile and loose) and partially because of the complicated algorithms for establishing and quantifying the 3D model. This study aimed to establish a workflow for processing CT images and constructing 3D pore models for Malan loess. The pore structure was then examined on the basis of 2D parameters from CT images and 3D parameters from the constructed 3D models.

2. Methodology

2.1Sampling and sample preparation

The samples of Malan loess used in this study were obtained from a slope in Yuci City, Shanxi, China. Undisturbed blocky samples (300 × 200 × 200 mm) were collected at a depth of 5.0 m to avoid plant roots. The in-situ orientation of the samples was clearly marked during sampling in the field. The samples were well sealed and carefully transported to the laboratory to avoid any disturbance. The dry density of the samples was 1.23 g/cm^3, the particle density was 2.70 g/cm^3, and the void ratio was 1.19. The clay (< 5 μm), silt (5–50 μm), and sand (> 50 μm) fractions accounted for 13.57%, 67.33%, and 19.10%, respectively. The above data of particle size analysis were obtained from a Malven Mastersizer2000 laser analyzer. After air-drying, five undisturbed blocky samples were trimmed into five cubes with edge length of 60 mm by a wire cutting machine. The original orientation of samples was unchanged. As shown in Fig. 1a, Z represents the in-situ vertical direction, and X and Y indicate the horizontal directions.

2.2 CT scanning

A nanoVoxel-2100 CT device (Fig. 1b; Sanying Precision Instruments Co., Ltd.) was used to scan the specimens. The scan system was set to 150 kV (voltage), 180 μA (current), and 0.2 s (exposure time). The CT device was equipped with a plate detector of 2000 × 2000 pixels. The X-ray beam width ("slice" thickness) was 59 μm. A series of 2D images with pixels of different gray values was obtained after processing projections (the remaining X-ray energy caught by the detector) by the built-in reconstruction algorithm of the CT system. The gray value of each pixel at the 2D images represents the X-ray attenuation coefficient of a certain point inside the specimen. Given the resolution of 59 μm, 1017 images (Fig. 1c) were obtained for each of the X, Y, and Z directions of a cubic specimen.

2.3 Data processing

A comprehensive scheme was established in this study for constructing the 3D model and deriving the parameters of the pore structure. Fig. 2 shows the flowchart, which consists of three main parts: 2D parameter extraction, 3D pore structure reconstruction, and 3D

parameter extraction. The relevant and efficient algorithms in the literature were cited and programmed in MATLAB to facilitate the flowchart.

Given the scanning resolution of 59 μm and the specimen size of 60 × 60 × 60 mm, each image obtained from CT scanning consisted of 1,034,289 (1017 × 1017) pixels with gray values in the range of 0–255 (Fig. 1c). The CT images for the center of the specimen usually have a higher gray level than those images at the boundaries. Therefore, applying a single threshold to all images introduces apparent bias in identifying solids and pores. To conduct segmentation (separate the image into pore and solid phases), the maximum entropy method proposed by Kapur et al. (1985) was adopted. The Kapur et al. (1985) method quantitatively considers the gray values of all pixels of an image, and assigns a unique threshold to each image (Luo et al., 2010). The pixels with gray values less than the threshold were identified as pores and colored white, whereas those with large gray values were solids and colored black.

The binary images obtained via segmentation were then analyzed to derive 2D pore parameters. The equivalent radius, length, and aspect ratio of pores were extracted using Malven image processing system, whereas the porosity and pore distribution entropy of each image were derived through a MATLAB program developed by us (Fig. 2). The equivalent radius is the radius of a circle with the same area as the pore. The length is the longest projection onto the major axis, with lines between any two points on the periphery of a pore. The major axis passes through the centroid of the pore, and the rotational energy along it is the minimum. The aspect ratio is equal to W/L (W and L are the equivalent width and length of pore, respectively). The equivalent width is equal to the ratio of pore area to pore length. The porosity is the ratio of the number of white pixels to the number of all pixels over a binary image.

A 3D pore model was constructed via stacking all binary images in one scanning direction by programming in MATLAB and removing the solid phase. As shown in Fig. 3a, the 3D pore model is a complicated network with dense connections and intersections of pores and pipes. The medial axis method (Lee et al., 1994), which is based on a thinning algorithm, was employed to isolate 3D pores and pipes. This algorithm iteratively erodes the voxels around each pore in six directions to obtain a one-voxel-wide medial axis. In each iteration, a voxel is removed if doing so does not change the overall topology of the pore structure. The above process yields a medial axis model (Fig. 3b), which consists of one-voxel-wide pore segments, and maintains the original topology of the pore structure. The method by Kerschnitzki et al. (2013) was employed to partition the medial axes into individual links by identifying the end points of each link.

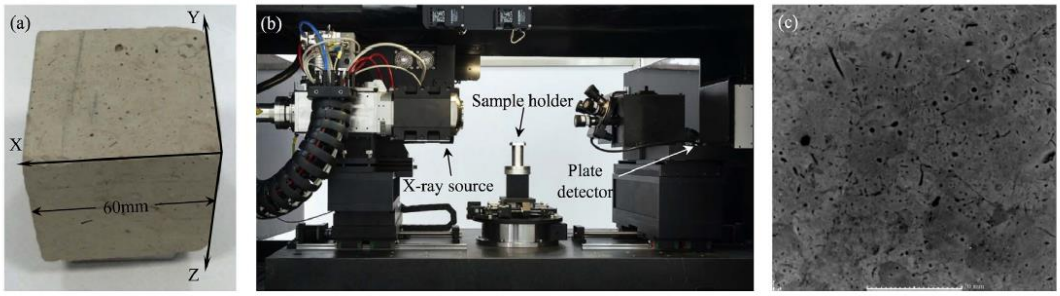

Fig. 1. Test set up: (a) specimen and the three directions for CT scanning; (b) the Sanying CT scan system used in this study; and (c) grey-scale image obtained from CT scanning.

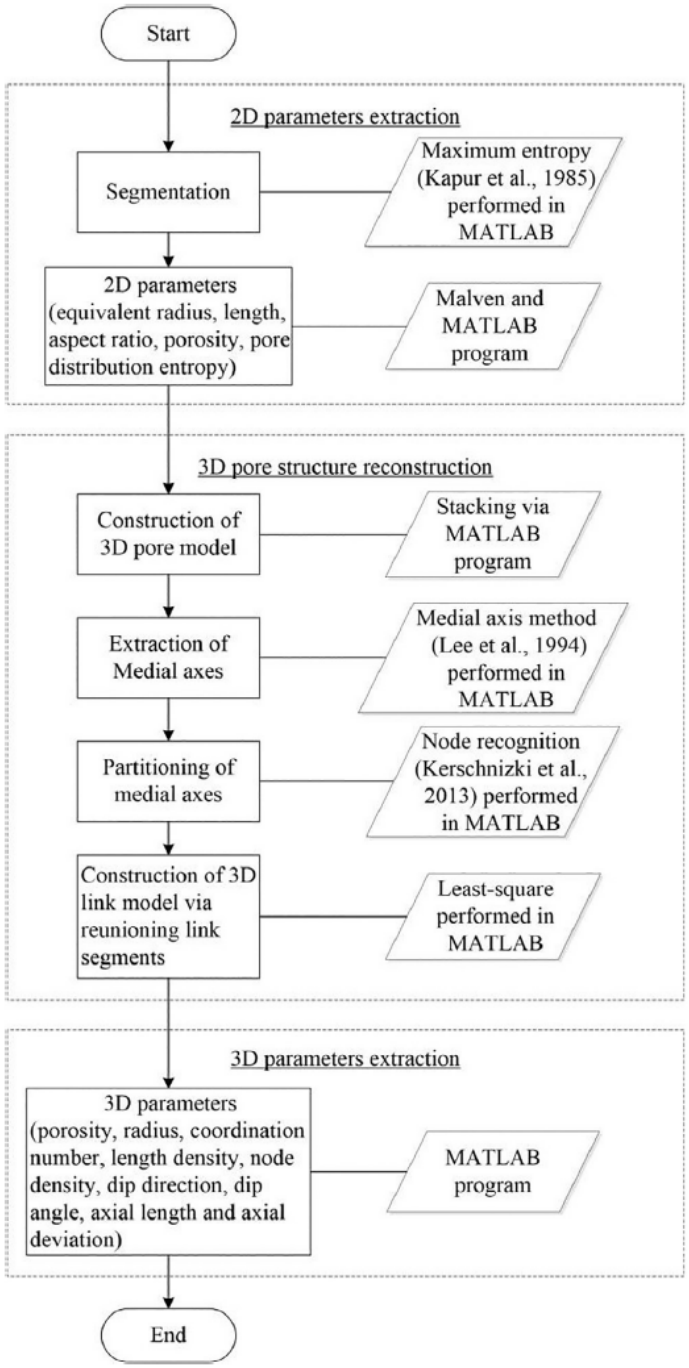

Fig. 2. The workflow for processing images from CT scan and constructing 3D structure models.

The center voxel of a template with 3 × 3 × 3 voxels was moved along the medial axis, and the number of voxels (n_v) on the medial axis that fell into the template (except the voxel under examination) was calculated. The voxel under examination was considered a cross node (yellow points in Fig. 4a), terminal node (blue points), or link node (black points) if the number (n_v) was greater than two, equal to one, or equal to two, respectively. The cross and terminal nodes were the separating nodes. The segment between the two separating nodes formed an individual link (Fig. 4a).

All nodes on each link were used to calculate the direction vector via least-square fitting. Any two links with the same cross node were considered a single link (the red line in Fig. 4b) if they shared the same direction vector. This process was conducted via a MATLAB program, and it created a 3D model composed of individual links.

The parameters depicting loess pore structure, such as porosity, coordination number, node density, pipe radius, length, length density, axial deviation, dip angle, and dip direction, were extracted using the 3D pore model and 3D link model constructed above. The porosity is the ratio of the number of pore voxels to the total number of voxels in the 3D pore model. The coordination number of a cross node is the number of links connected with the cross node. The length density (cm/ cm^3) is the ratio of the summation of lengths of all links to the total volume of the 3D pore model. The node density (no./cm^3) is the ratio of the total number of cross nodes to the volume of the 3D pore model. The pipe radius is the average of distances between each node on the link to its closest node on the pipe surface. The axial length is the length of the link's axis. The link's axis is the least-square fitted line of the link. The axial deviation (D) of links is calculated according to $D = 1\text{-}L_v/L_r$ (L_v is the axial length of link, and L_r is the true length). Axial deviation reflects the curvature of a link. A perfectly straight link would have a D of 0, whereas an extremely curved link would have a D close to 1. Dip angle (α) and dip direction ( ) of links were defined and calculated according to Fig. 4c.

3. Results

3.1. Macropores discovered by 2D images

Five representative images (slices) with a spacing of 10 mm were collected along the X direction to stack into a sequence, as shown in Fig. 5a. The same was done for the Y and Z directions (Fig. 5b and c). The image perpendicular to the X direction was defined as X image, whereas those perpendicular to the Y and Z directions were defined as Y and Z images, respectively. According to Fig. 5, it is found that (1) pores on X and Y images were unevenly distributed with local dense and sparse distributions, whereas pores showed even distribution on Z images; (2) pores on both X and Y images varied in shape and size (round or elongated tube-shaped pores), whereas pores on Z images were almost round or semi-round with similar sizes; and (3) pores on Z images formed pipes throughout the whole specimen as indicated by the thick dashed line, whereas pores on X and Y images showed no clear connectivity.

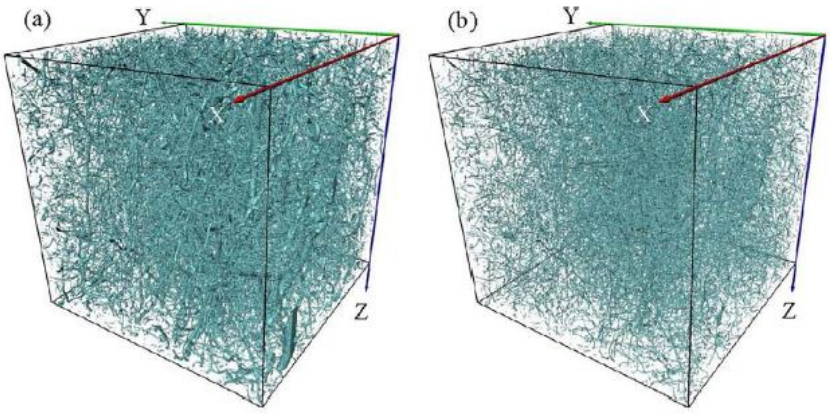

Fig. 3. 3D macropore structure of Malan loess: (a) 3D pore model; and (b) 3D medial axis model.

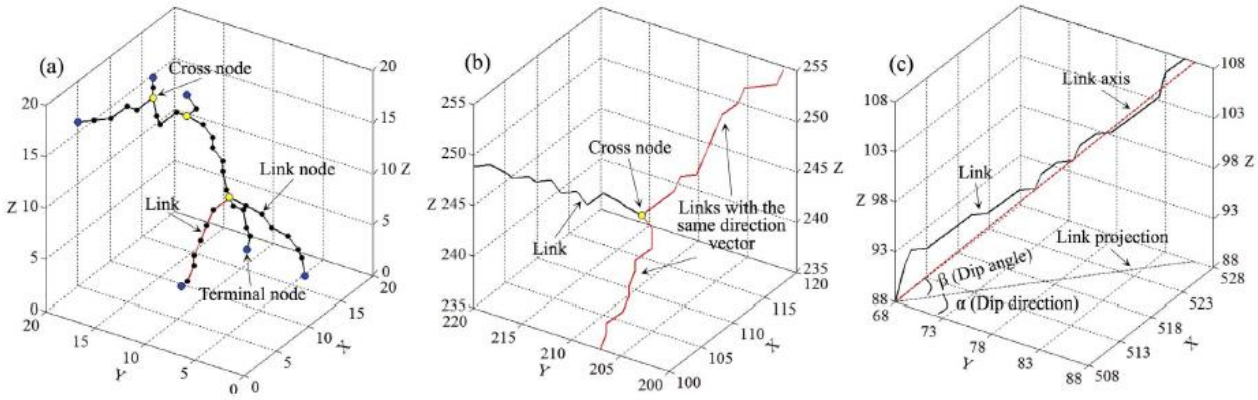

Fig. 4. Partitioning the medial axis: (a) definition of nodes; (b) reunion of links with the same direction vector; and (c) definition of dip angle and dip direction of pipes.

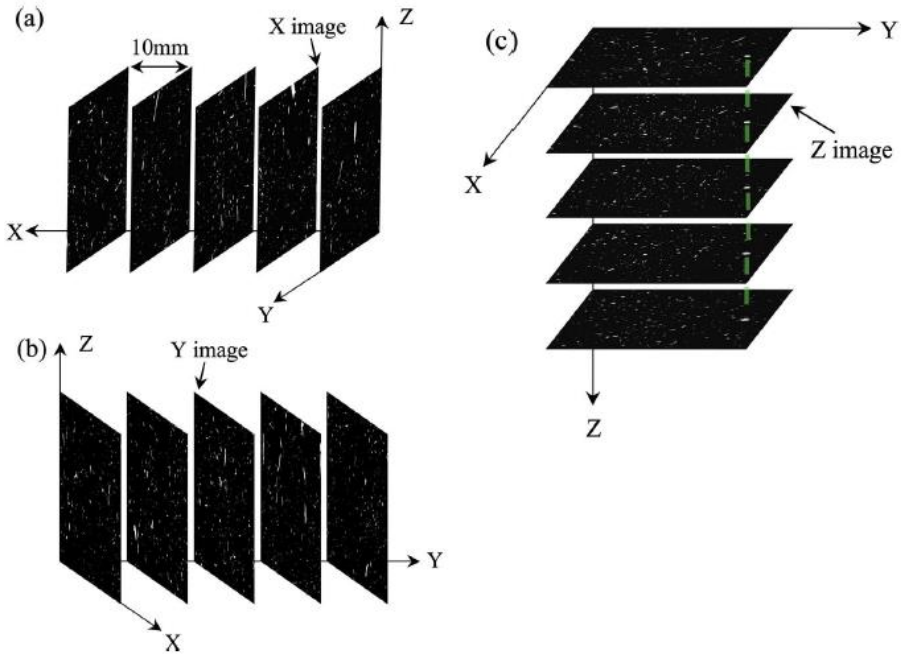

Fig. 5. Five images of equal spacing stacked in: (a) the X; (b) Y; and (c) Z directions. (green dashed line indicates a good connectivity of pores in the Z direction). (For interpretation of the references to colour in this figure legend, the reader is referred to the web version of this article.)

Table 1
Radius and length of pores discovered from 2D images in different directions.

Direction	Parameter							
	Radius				Length			
	Mean (μm)	STD	Max (μm)	Range (μm)	Mean (μm)	STD	Max (μm)	Range (μm)
X images	183	142	3656	3592	577	700	20,849	20,531
Y images	185	148	3564	3504	590	714	20,810	20,492
Z images	190	131	2189	1902	563	487	9646	9528

Note: STD – standard deviation; Max – maximum value; and Range – difference between maximum and minimum values.

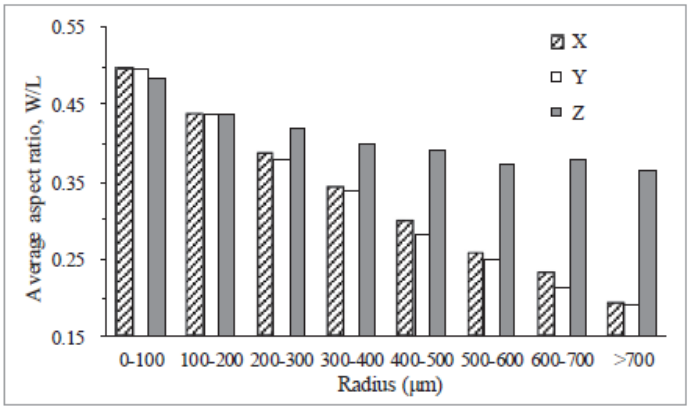

Fig. 6. Changes of average aspect ratios of pores with radius for each of the X, Y and Z direction.

Table 1 lists the statistics of the pore sizes in each direction. The range (maximum-minimum) of equivalent radius of pores on Z images was 1902 μm, which was much less than that in the other two directions (about 3500 μm). In addition, the lengths of pores on Z images fell into a very narrow range compared with the other two directions. This result was consistent with Fig. 5, where large pores were evident in the X and Y directions, whereas the sizes of pores in the Z direction were quite uniform. Fig. 6 shows the average aspect ratio of each fraction of pore radius. The aspect ratio of pores decreased from 0.49 to 0.18 in the X and Y directions as the pore radius increased. However, the aspect ratio of pores in the Z direction was generally greater than 0.4, and it remains almost constant for pores greater than 300 μm. The above observation indicates that pores in the Z direction were quite equal-dimensional and uniform in shape, whereas pores in the X and Y directions varied in shape to a great extent and the large ones were elongated.

Fig. 7a shows the calculated porosity for images in each direction. The porosity varied from image to image along each of the three directions. However, the variation was limited along the Z direction (with a variance of 0.03) compared with those along the X (0.27) and Y (0.20) directions. This result indicates a relatively constant distribution of pores along the Z direction and arbitrary distributions along the X and Y directions. The pore distribution entropy (Pd) was introduced in this study to reflect the spatial uniformity of pores distributed on each image. Pd was calculated according to $E = \sum_{n}^{i=1} P_i \times \ln P_i$ (P is the porosity of a section, and n is the number of sections over each binary image). Pd was 1 if the pores were evenly distributed on the image, and it was a small value if the pores were distributed

in clusters. As shown in Fig. 7b, the pore distribution entropies of Z images (with a mean of 0.856) were greater than those of X (0.733) and Y (0.712) images, indicating that pores were distributed more evenly in the Z direction than in the other two directions.

3.2. 3D pore structure

The overall porosity calculated from the reconstructed 3D pore model was 2.18%, which was consistent with the average value calculated from 2D images in any of the three directions. The total number, total length, number density, and length density of pipes in the reconstructed 3D model were 33072, 4034.23 cm, 153 no./cm^3, and 28.68 cm/cm^3, respectively. The total number and density of cross node in the constructed model were 14686 and 168 no./cm^3, respectively. The average coordination number of cross node was 3.15, which suggests that more than three pipes were connected to the same cross node. The above values, especially the average ones, indicate the Malan loess is porous with a complicated and dense network of pores and pipes.

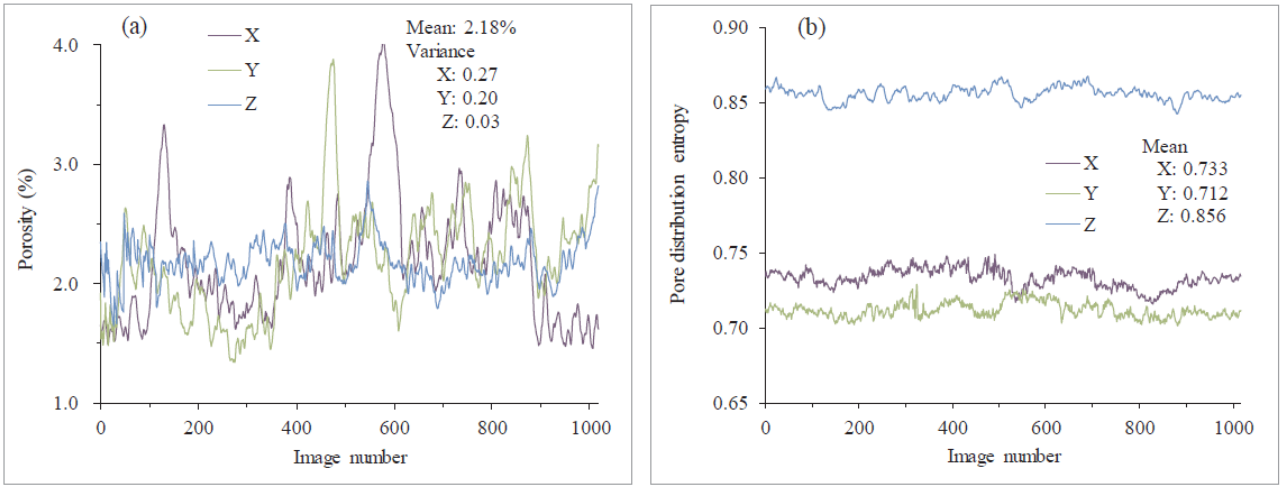

Fig. 7. Pore characteristics derived from 2D images of CT scanning along each of the three directions: (a) porosity; and (b) pore distribution entropy.

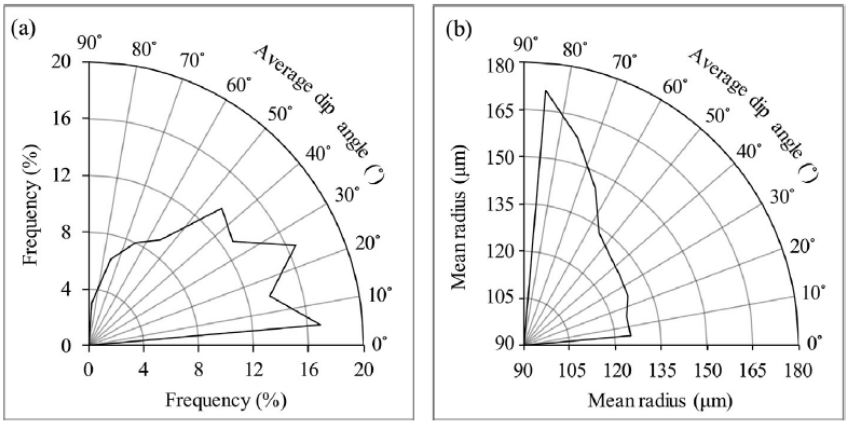

Fig. 8. Dip angles of pipes in Malan loess shown in rose diagrams: (a) frequency distribution of average dip angles; and (b) variation of average dip angles with mean radius of pipes.

Dip angles of all pipes were calculated according to Fig. 4c, and the frequency distribution of these angles was plotted in a rose diagram (Fig. 8a). The rose diagram was divided into nine zones, each with a span of 10°. The average dip angle of pipes falling within the same zone was assigned to that zone. The frequency was calculated by taking the number of pipes in each zone divided by the total number. As shown in Fig. 8a, most pipes were concentrated in the range of 5–45°. However, the pipes with large radius were aligned vertically, whereas the thin pipes were aligned at gentle angles (Fig. 8b).

Fig. 9a shows the whole view of the constructed 3D pore model for the tested Malan loess specimens. The pipes were mainly round, similar to a curved cylinder. They were interconnected with each other, generating a complex and dense network. The pipes with dip angles in the range of 0–45° and dip direction in ranges of 135–225°, 315–360°, or 0–45° were extracted from Fig. 9a to compose Fig. 9b. Thus, this model mainly consisted of pipes aligned in the X direction. The same was conducted for pipes aligned in the Y direction (Fig. 9c) by using pipes with dip angles in the range of 0–45° and dip directions in ranges of 45–135° or 225–315°. This procedure was also repeated for the Z direction using pipes with dip angle in the range of 45–90° (Fig. 9d). Our results revealed that (1) pipes aligned in the Z direction were long and had the best conductivity compared with those in the other two directions; (2) pipes in the Z direction were generally straight, whereas those in the other two directions were curved; and (3) a great number of thick pipes was found in the Z direction, whereas pipes in the other two directions were much thinner.

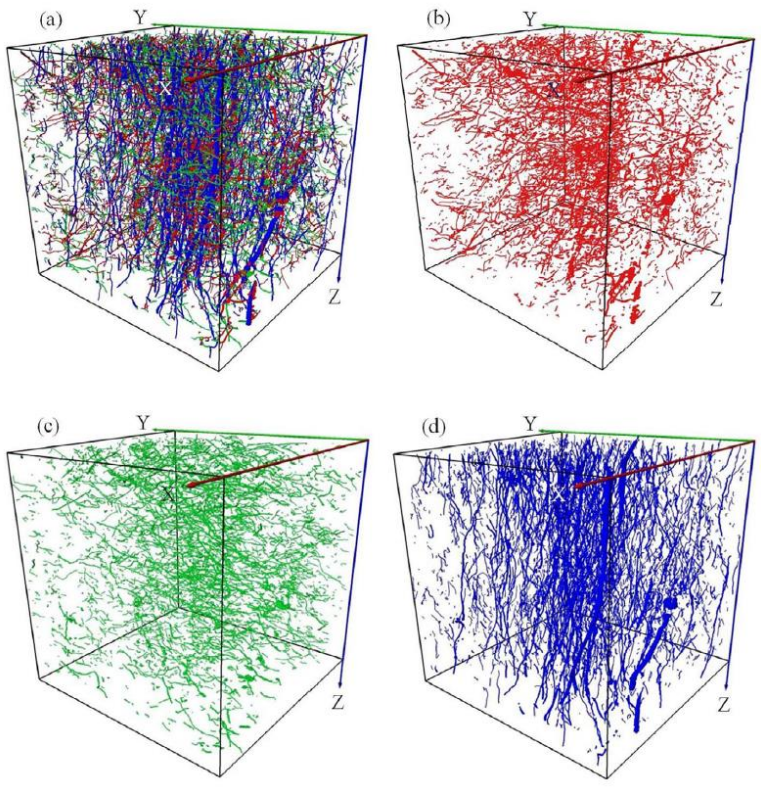

Fig. 9. 3D structure models of Malan loess with: (a) all pipes; (b) pipes in the X direction; (c) pipes in the Y direction; and (d) pipes in the Z direction.

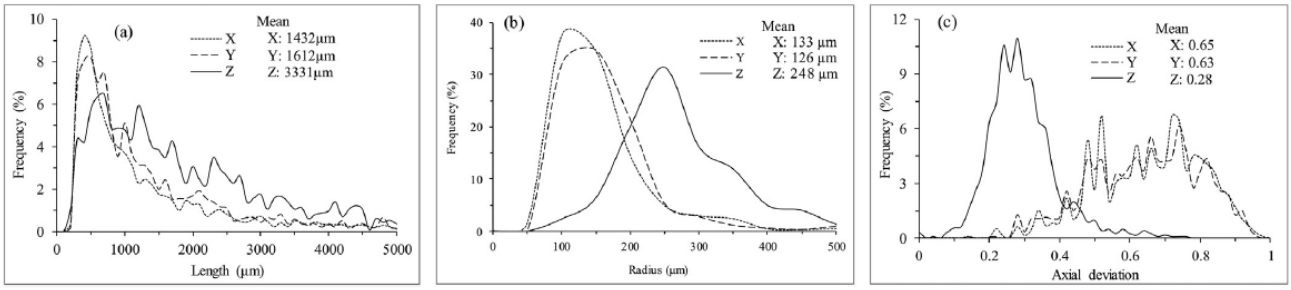

Fig. 10. Frequency distribution of: (a) pipe length; (b) pipe radius; and (c) axial deviation of pipes in the X, Y and Z directions.

The above observations were in good agreement with the statistical analysis on the geometry of pipes (Fig. 10). The average length of pipes aligned in the Z direction was 3331 μm, which was much greater than that in the other two directions (X, 1432 μm; and Y, 1612 μm). As shown in Fig. 10a, the pipes with radius greater than 1500 μm still accounted for a large percentage of all pipes in the Z direction, whereas pipes in the other two directions were concentrated in the range below 1500 μm. The pipes aligned in the Z direction were generally thicker (with an average radius of 248 μm) than those in the other two directions (with an average radius of about 130 μm) (Fig. 10b). Fig. 10c shows that the pipes in the Z direction were straight with an average axial deviation of 0.28, whereas those in the other directions were curved with much greater deviation (0.65 and 0.63 in the X and Y directions, respectively).

4. Discussion

The abovementioned results demonstrate that Malan loess is an anisotropic geological material. It is characterized by (1) a dense and complex network of pipes and pores (cross node density of 168 no./ cm^3; pipe length density of 28.68 cm/cm^3); (2) different appearance of pores in varying directions; and (3) a strongly anisotropic pipe structure. This statement can be supported by examining 2D images and 3D pore structural models. In 2D vision, pores in the vertical direction were round and obeyed a spatially uniform distribution, whereas those in the other two directions strongly varied in shape and were distributed in clusters. In 3D vision, the pipes in the Z (vertical) direction were thick, long, and straight, but those in the other two directions were curved and erratic in radius and length.

We conducted numerical simulation and laboratory tests on the permeability of Malan loess in three orthogonal directions (X, Y, and Z). The 3D pore model reconstructed from CT images was imported into AVIZO program for numerical simulation. The initial conditions were set (input pressure = 110 kPa, output pressure = 100 kPa, and fluid viscosity = 0.001 Pa·s). The laboratory experiments involved nine undisturbed cylindrical specimens with a diameter of 61.8 mm and a height of 40 mm. Three specimens were in the X direction, three were in the Y direction, and the remaining three were in the Z direction. These nine specimens were all cut from the loess blocks, which were used for preparing CT scanning specimens. The permeability tests were conducted in a TS-50 falling head device in

accordance with Chinese standard SL237-1999 (The Ministry of Water Resource of the People's Republic of China, 1999).

The seepage channels in the numerical simulation by AVIZO are shown in Fig. 11. Seepage in the Z (Fig. 11c) direction prevailed over that in the other two directions (Fig. 11a and b). The seepage channels were concentrated in the Z direction. These channels not only facilitated fluent paths for water travelling in the Z direction but also worked as connectors for forming flow paths in the X and Y directions. As shown in Fig. 12, the permeability coefficients in the Z direction were significantly greater than those in the other two directions. This finding was consistent with the results reported by Liang et al. (2012), who found that permeability in the vertical direction of Malan loess is two to three times that in the horizontal directions. The laboratory tests agreed well with the numerical simulation and showed the same trend of permeability in different directions. The difference in magnitude of the measured permeability coefficients between numerical simulation and laboratory tests was partially because the micropores (< 59 μm) were not identified by the present CT scanning and did not participate in AVIZO simulation, and partially because the AVIZO program could not enlarge or create seepage channels during calculation.

After the accumulation of windblown dust, loess experiences a long period of structural evolution, called loessification (Smalley et al., 2011). The functions of water, dry–wet cycling, freezing–thawing, and temperature fluctuation are believed to be the main forces that drive the loessification process (Zeng et al., 2015; Smalley and Marković, 2014).

Moisture in loess mainly comes from precipitation, frost, and snow (Sun and Ma, 2015; Zhang et al., 2012; Liu, 2016). Rainwater, as the main source, can infiltrate to a depth of 1 to several meters in loess (Tan et al., 2017; Yang et al., 2015). On one hand, the water seepage in loess takes away small soil particles to depth and facilitates the formation of pipes in loess (Verachtert et al., 2010). On the other hand, the infiltrating water dissolves soluble salts, causing transportation and reprecipitation of cements (e.g., calcium carbonates; Smalley et al., 2006) and reinforcement of existing pipes or pores by cements (Dijkstra et al., 1995; Cilek, 2001). The evaporation of water due to dry climate also contributes in the same way as water moves upwards. All functions above worked in the vertical direction, making the pipes vertically aligned.

The average annual precipitation in the LPC ranges from 450 nm to 720 mm, and precipitation is mainly concentrated in summer in the form of rainstorm (Zhuang et al., 2017). The annual potential evaporation in this area is about 1649 mm (Yang et al., 2012). Such a semi-arid and arid climate favors dry–wet cycling in loess (Sun and Ma, 2015). During drying, the increase in matric suction and attraction between particles in loess cause tensile stress (τ), leading to tensile fracturing. As the vertical stress (σ_1) is generally greater than the horizontal one (σ_2) due to the overlaying soil layers, tensile fracturing more likely occurs horizontally, which facilitate the formation of vertical cracks or pipes (Li et

al., 2014; Ye et al., 2016). The cracks induced by wetting/drying can occasionally extend to 70 mm depth (Adeniji, 1991; Goehring et al., 2010).

Frequent freezing/thawing is another cause for cracks in loess. The frozen depth in LPC reaches more than 1 m (Zeng et al., 2015). The meltwater in daytime of winter penetrates into the loess and works similar to rainwater to create vertical pipes or pores (Konrad, 1989). The meltwater, once penetrates into loess, will become frozen at low temperatures at night in winter (about −20 °C, China National Meteorological Center). This phenomenon introduces tensile fracturing due to the volume expansion, and vertically aligned cracks are formed (Chamberlain and Gow, 1979).

The temperature in loess areas (e.g., the LPC) fluctuates dramatically within a year or a day. The daily variation in temperature in summer is about 15 °C, whereas that in winter can be about 25 °C (China National Meteorological Center).

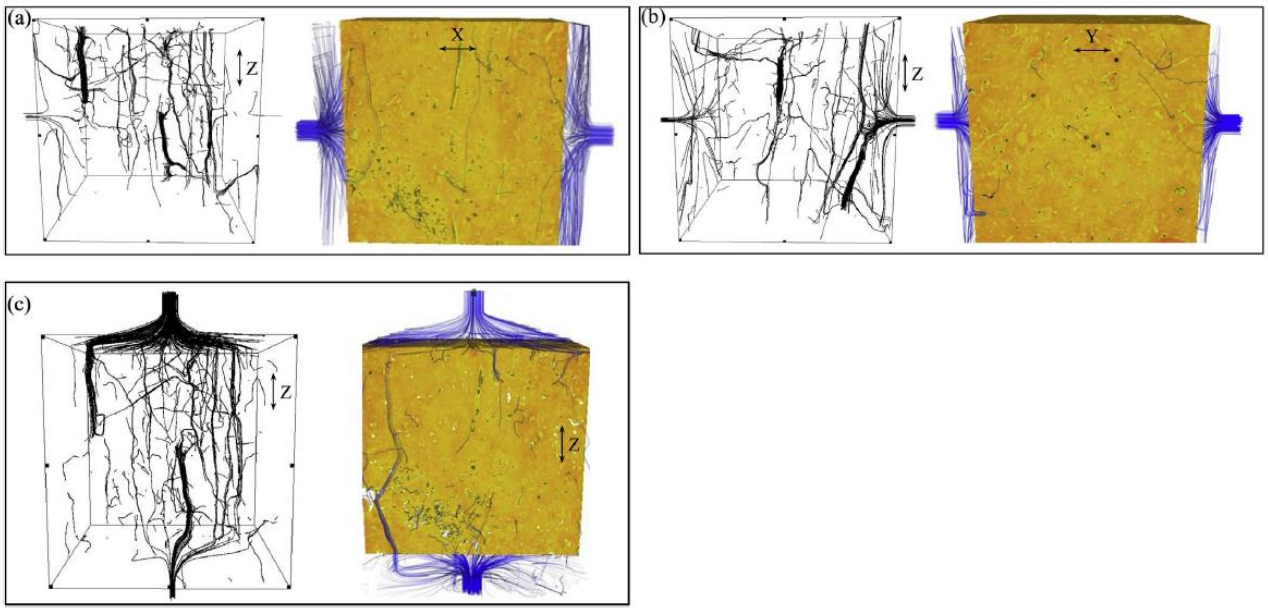

Fig. 11. Seepage channels in the numerical simulation by AVIZO in the: (a) X; (b) Y; and (c) Z directions. (The yellow part represents loess). (For interpretation of the references to colour in this figure legend, the reader is referred to the web version of this article.)

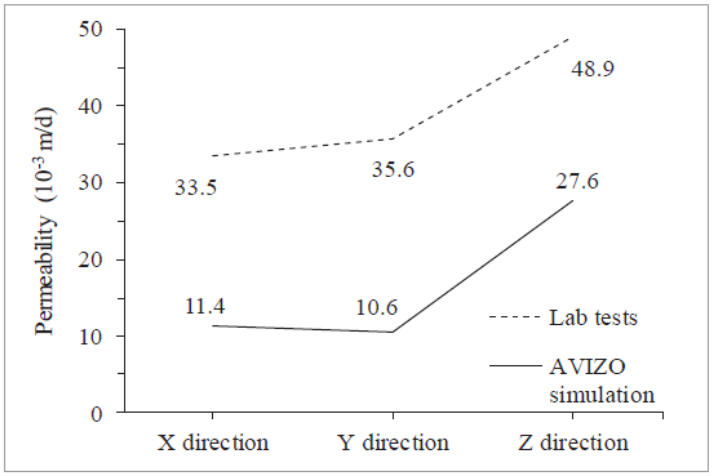

Fig. 12. Permeability coefficients of Malan loess obtained from laboratory tests and AVIZO simulation.

As loess contains clay minerals (e.g., kaolinite, montmorillonite, and chlorite), accounting for about 20% in volume (Galović et al., 2006), the rapid, dramatic temperature changes induce swelling/contraction of loess (Mao et al., 2013), which in turn results in tensile fracturing in loess and vertically aligned cracks and pipes.

5. Conclusions

This study investigated the pore structure of Malan loess in the LPC. Undisturbed cubic specimens of 60 × 60 × 60 mm were scanned by CT technique. This study aimed to establish a sophisticated and efficient workflow by selecting and performing relevant mathematical algorithms in MATLAB, such as the maximum entropy method, medial axis method, and node recognition algorithm. This workflow deals with processing of CT images for the construction of 3D pore models, and it can identify and separate individual pipes within the model by partitioning and recombining links. This workflow facilitates analysis on the Malan loess structure by quantifying its characteristics, such as radius, length, axial deviation, dip angle, and dip direction of pipes. Results revealed that Malan loess is a strongly anisotropic geological material. It is characterized by a dense and complex network of pores and pipes. The pores discovered by horizontal slices were round and relatively uniform in shape and size. They were evenly distributed on horizontal planes. The pores discovered by vertical slices varied in shape and size, and they were distributed in clusters on vertical planes. The pores showed good connectivity in the vertical direction to form vertically aligned pipes but displayed weak connectivity in the other two directions. The pipes in the vertical direction were thick, long, and straight compared with those in the other two directions. These findings were in good agreement with numerical simulation and laboratory permeability tests, which indicate a greater permeability in the vertical direction than in the other two directions.

There is a conflict between the specimen size and the scanning resolution. Given a certain CT device, a large specimen will result in low resolution. Considering that Malan loess are rich in macropores, small specimens cannot encompass macropores and are not

representative. Thus, this study used specimens of 60 × 60 × 60 mm in size. However, such a specimen could only allow a scanning resolution of about 60 μm according to modern CT techniques. This restriction has hindered the identification of pores smaller than this size, and makes the conclusions drawn in this study limited to macropores. Future work may be justified to examine the micropore structure of Malan loess and incorporate both micro- and macro-pores in numerical simulation.

Acknowledgements
This study was supported by the 2014 Fund Program for the Scientific Activities of Selected Returned Overseas Professionals in Shanxi Province, Shanxi Scholarship Council of China, Outstanding Innovative Teams of Higher Learning Institutions of Shanxi, Soft-science Fund Project of Science and Technology in Shanxi, Research Project for Young Sanjin Scholarship of Shanxi, Collaborative Innovation Center for Geohazard Process and Prevention at Taiyuan Univ. of Tech., Recruitment Program for Young Professionals of China.

References

Adeniji, F.A., 1991. Recharge function of vertisolic vadose zone in sub-shelian Chad Basin. Proc. of 1st Inter. Conf. on Aarid Zone Hydrogeology, Hydrology and Water Resources. Maiduguri, pp. 331–348.

Cai, J., Dong, B.Y., 2011. Micro-structure study on collapsibility loess with SEM method. Appl. Mech. Mater. 52–54, 1279–1283.

Chamberlain, E.J., Gow, A.J., 1979. Effect of freezing and thawing on the permeability and structure of soils. Eng. Geol. 13 (1), 73–92.

Cilek, V., 2001. The loess deposits of the Bohemian Massif: Silt provenance, Palaeometeorology and loessification processes. Quatern. Int. 76–77 (1), 123–128.

Deng, J., Wang, L.M., Zhang, Z.Z., 2007. Microstructure characteristics and seismic subsidence of loess. Chinese J. Geotech. Eng. 29 (4), 542–548 (in Chinese).

Dijkstra, T.A., Smalley, I.J., Rogers, C.D.F., 1995. Particle packing in loess deposits and the problem of structure collapse and hydroconsolidation. Eng. Geol. 40 (1–2), 49–64.

Galović, L., Mileusnić, M., Peh, Z., Durn, G., Halamić, J., 2006. Mineralogical and geochemical characteristics of loess/paleosol section in Šarengrad, Srijem, Croatia. In: Vlahović, I., Tibljaš, D., Durn, G., Biševac, V. (Eds.), 3rd Mid-European Clay Conference.

Gao, G., 1988. Formation and development of the structure of collapsing loess in China. Eng. Geol. 25 (2–4), 235–245.

Goehring, L., Conroy, R., Akhter, A., Clegg, W.J., Routh, A.F., 2010. Evolution of mud-crack patterns during repeated drying cycles. Soft Matter 6 (15), 3562–3567.

Hu, R.L., Yeung, M.R., Lee, C.F., Wang, S.J., 2001. Mechanical behavior and micro-structural variation of loess under dynamic compaction. Eng. Geol. 59 (3–4), 203–217.

Kapur, J.N., Sahoo, P.K., Wong, A.K.C., 1985. A new method for gray-level picture thresholding using the entropy of the histogram. Comput. Vision Graph. Image Process. 29 (3), 273–285.

Kerschnitzki, M., Kollmannsberger, P., Burghammer, M., Duda, G.N., Weinkamer, R., Wagermaier, W., Fratzl, P., 2013. Architecture of the osteocyte network correlates with bone material quality. J. Bone Mineral Res. Off. J. Am. Soc. Bone Mineral Res. 28 (8), 1837–1845.

Konrad, J.M., 1989. Physical processes during freeze-thaw cycles in clayey silts. Cold Reg. Sci. Technol. 16 (3), 291–303.

Lee, T.C., Kashyap, R.L., Chu, C.N., 1994. Building Skeleton Models via 3-D Medial Surface/Axis Thinning Algorithms, vol. 56, no. 6, Academic Press, Inc., pp. 462–478.

Lei, X.Y., 1988. The types of loess pores in China and their relationship with collapsibility. Sci. Sinia. Series B. 31 (11), 1398–1411.

Li, T.L., Wang, H., Fu, L.K., Liang, Y., 2014. Test simulation on the forming mechanism of loess vertical joints. J. Earth Sci. Environ. 36 (2), 127–134 (in Chinese).

Li, P., Vanapalli, S., Li, T., 2016. Review of collapse triggering mechanism of collapsible soils due to wetting. J. Rock Mech. Geotech. Eng. 8 (2), 256–274.
Li, Z.T., Lu, D.M., Cai, Y.D., Ranjith, P.G., Yao, Y.B., 2017. Multi-scale quantitative characterization of 3-D pore-fracture networks in bituminous and anthracite coals using FIB-SEM tomography and X-ray μ-CT. Fuel 209, 43–53.
Liang, Y., Xing, X.L., Li, T.L., Xu, P., Liu, S.L., 2012. Study of anisotropic permeability and mechanism of Q3 loess. Rock Soil Mech. 33 (5), 37–42 (in Chinese).
Lin, R.S., 1990. Analysis of microstructure, pore structure and permeability of loess in Weibei, China. Shaanxi Water Resour. 2, 43–47 (in Chinese).
Liu, H.M., 1999. Computed image processing method of loess porosity micro-structure. Earthq. Res. Plateau. 11 (3), 44–48 (in Chinese).
Liu, Y.F., 2016. Spatial and temporal variation of different precipitation type in the Loess Plateau area. Sci. Geograph. Sin. 36 (8), 1227–1233 (in Chinese).
Luo, L.F., Lin, H., Li, S.C., Lin, H., Flühler, H., Otten, W., 2010. Quantification of 3-d soil macropore networks in different soil types and land uses using computed tomography. J. Hydrol. 393 (1), 53–64.
Mao, H., Qiu, Z.S., Huang, W.A., Shen, Z.H., Yang, L.Y., Zhong, H.Y., 2013. The effects of temperature and pressure on the hydration swelling characteristics of clay mineral. Petrol. Drill. Tech. 41 (6), 56–61 (in Chinese).
Matalucci, R.V., Abdel-Hady, M., Shelton, J.W., 1970. Influence of microstructure of loess on triaxial shear strength. Eng. Geol. 4 (4), 341–351.
Ng, C.W.W., Mu, Q.Y., Zhou, C., 2017. Effects of soil structure on the shear behaviour of an unsaturated loess at different suctions and temperatures. Can. Geotech. J. 54 (2).
Perret, J., Prasher, S.O., Kantzas, A., Langford, C., 1999. Three-dimensional quantification of macropore networks in undisturbed soil cores. Soil Sci. Soc. Am. J. 63, 1530–1543.
Smalley, I.J., Mavlyanova, N.G., Rakhmatullaev, K.L., Shermatov, M.S., Machalett, B., Dhand, K.O., Jefferson, I.F., 2006. The formation of loess deposits in the Tashkent region and parts of Central Asia; and problems with irrigation, hydrocollapse and soil erosion. Quat. Int. 152 (3), 59–69.
Smalley, I., Marković, S.B., Svirčev, Z., 2011. Loess is [almost totally formed by] the accumulation of dust. Quat. Int. 240 (1), 4–11.
Smalley, I.J., Marković, S.B., 2014. Loessification and hydroconsolidation: There is a connection. Catena 117 (3), 94–99.
Sun, C., Ma, Y., 2015. Effects of non-linear temperature and precipitation trends on Loess Plateau droughts. Quat. Int. 372, 175–179.
Tan, T.K., 1988. Fundamental properties of loess from Northwestern China. Chinese J. Geotech. Eng. 25 (2–4), 103–122.
Tan, H., Liu, Z., Rao, W., Jin, B., Zhang, Y., 2017. Understanding recharge in soil-groundwater systems in high loess hills on the Loess Plateau using isotopic data. Catena 156, 18–29.

Terzaghi, K., Peck, R.B., Mesri, G., 1996. Soil Mechanics in Engineering Practice, fifth ed. Wiley, New York, pp. 592.

The Ministry of Water Resource of the People's Republic of China, 1999. L237-1999 Specification of Soil Test. (in Chinese).

Verachtert, E., Eeckhaut, M.V.D., Poesen, J., Deckers, J., 2010. Factors controlling the spatial distribution of soil piping erosion on loess-derived soils: A case study from central Belgium. Geomorphology 118 (3–4), 339–348.

Yang, B.H., Ai-Xiang, W.U., Miao, X.X., Liu, J.Z., 2014. 3D characterization and analysis of pore structure of packed ore particle beds based on computed tomography images. Trans. Nonferrous Met. Soc. China 24 (3), 833–838.

Yang, L., Wei, W., Chen, L., Mo, B., 2012. Response of deep soil moisture to land use and afforestation in the semi-arid Loess Plateau, China. J. Hydrol. 475 (6), 111–122.

Yang, X., Jiang, W., Yang, S., Kong, Z., Luo, Y., 2015. Vegetation and climate changes in the western Chinese Loess Plateau since the Last Glacial Maximum. Quat. Int. 372 (7), 58–65.

Yang, Y.L., 1989. Study of the mechanism of loess collapse. Sci. China (Series B) 32 (5), 94–107.

Ye, W.J., Li, C.Q., Ma, W.C., 2016. Mechanism fractured loess expansion joints under the effects of wet-dry cycle. Sci. Technol. Eng. 16 (30), 122–127 (in Chinese).

Zeng, L., Zhang, G.Z., Hu, W., Huang, J.T., 2015. Spatial variation characteristics of temperature and moisture in shallow loess layer under freezing-thawing condition. Geol. Bull. China 34 (11), 2123–2131 (in Chinese).

Zhang, Q., Wang, S., Wen, X.M., Nan, Y.H., Zeng, J., 2012. An experimental study of land surface condense phenomenon and water budget characteristics over the Loess Plateau. Acta Meteorol. Sin. 70 (1), 128–135 (in Chinese).

Zhou, H., Peng, X., Perfect, E., Xiao, T., Peng, G., 2013. Effects of organic and inorganic fertilization on soil aggregation in an Ultisol as characterized by synchrotron based X- ray micro-computed tomography. Geoderma 195–196 (1), 23–30.

Zhu, H.Z., 1963. Characteristics of particle and structure of loess from the middle reaches of Yellow River by observation the oil soaked polished section. Sci. Geol. Sin. 4 (2), 88–100 (in Chinese).

Zhuang, J., Peng, J., Wang, G., Javed, I., Wang, Y., Li, W., 2017. Distribution and characteristics of landslide in Loess Plateau: A case study in Shaanxi province. Eng. Geol.